applied sciences

MDPI

Article

Terahertz Spectroscopic Characterization of a Daidzein-Piperazine Crystalline Solid Form Prepared by Liquid-Assisted Grinding

Zhipeng Wang [1,2,3], Haofei Sun [1,2,3], Hailin Cui [1,2,3,*], Shengbo Zhang [1,2,3], Bo Su [1,2,3] and Cunlin Zhang [1,2,3]

[1] Department of Physics, Capital Normal University, Beijing 100048, China; 2250602044@cnu.edu.cn (Z.W.); 2240602039@cnu.edu.cn (H.S.); zhangshengbo@cnu.edu.cn (S.Z.); su-b@163.com (B.S.); zclcnu@163.com (C.Z.)
[2] Beijing Key Laboratory for Terahertz Spectroscopy and Imaging, Beijing 100048, China
[3] Key Laboratory of Terahertz Optoelectronics, Ministry of Education, Beijing 100048, China
* Correspondence: hailincui@126.com

Abstract

Daidzein is a natural flavonoid with low aqueous solubility and bioavailability. The low-frequency terahertz spectroscopic characteristics and corresponding vibrational origins of the 1:1 daidzein–piperazine (DAI–PIP) crystalline system remain insufficiently explored. In this study, a DAI–PIP crystalline solid form was prepared by liquid-assisted grinding at a 1:1 starting-material molar ratio and characterized using powder X-ray diffraction (PXRD), differential scanning calorimetry–thermogravimetric analysis (DSC–TGA), terahertz time-domain spectroscopy (THz-TDS), and scanning electron microscopy (SEM). The experimental PXRD pattern exhibited characteristic reflections at 18.62° and 23.19°, while several reflections of the starting materials were absent. The good overall agreement between the experimental and simulated PXRD patterns supported the reasonableness of the periodic crystal-structure models used for the subsequent THz calculations. DSC–TGA revealed distinct endothermic events and multistage mass-loss behavior, while SEM showed finer and relatively uniform particle aggregates after grinding. The DAI–PIP product exhibited experimental THz absorption features at approximately 1.46, 1.84, and 2.28 THz. Periodic DFT calculations reasonably reproduced the principal experimental features. The calculated mode at 1.89 THz was mainly localized on the hydroxyl-substituted aromatic ring of DAI, whereas the modes at 1.35 and 2.20 THz involved coupled motions of DAI and PIP accompanied by intermolecular N–H···O hydrogen-bond deformation. These results provide a structurally supported interpretation of the characteristic low-frequency vibrations of the DAI–PIP crystalline system and demonstrate the value of combining THz-TDS with periodic DFT calculations for investigating its solid-state vibrational behavior.

Keywords: terahertz time-domain spectroscopy; pharmaceutical multicomponent solid; anhydrous piperazine; daidzein

Check for updates

Academic Editor: Mira Naftaly

Received: 3 July 2026
Revised: 1 September 2026
Accepted: 6 September 2026
Published: 8 September 2026

Copyright: © 2026 by the authors. Licensee MDPI, Basel, Switzerland. This article is an open access article distributed under the terms and conditions of the Creative Commons Attribution (CC BY) license.

1. Introduction

Cocrystals are single-phase crystalline materials composed of two or more molecular species in a defined stoichiometric ratio and assembled through noncovalent interactions, including hydrogen bonding, van der Waals forces, and π–π stacking [1–3]. In pharmaceutical science, a pharmaceutical cocrystal typically comprises an active pharmaceutical ingredient (API) and a coformer [4,5]. Cocrystallization can modify properties such as

dissolution rate, solubility, and physical stability without changing the covalent structure of the API, making it a useful strategy in drug formulation and solid-form development.

Daidzein (7,4′-dihydroxyisoflavone, DAI) is a natural flavonoid widely distributed in leguminous plants [6]. It has been associated with anti-inflammatory, anticancer, and antidiabetic activities [7], as well as potential effects in osteoporosis, hypertension, and coronary heart disease [8,9]. However, its tightly packed crystal structure limits solvent penetration and contributes to low aqueous solubility [6]. Daidzein is classified as a Biopharmaceutics Classification System Class IV compound because of its low solubility and low permeability [10], which constrain its pharmaceutical development. Solid-form strategies that address these properties may therefore improve its formulation potential.

Anhydrous piperazine (PIP) is a symmetric nitrogen-containing heterocycle with two secondary amine nitrogen atoms that can participate in hydrogen bonding [11]. Daidzein contains phenolic hydroxyl groups and a carbonyl group, providing complementary hydrogen-bond donor and acceptor sites for association with piperazine [6]. Piperazine is water-soluble and has been used as a coformer or ligand in several pharmaceutical multicomponent systems [6,11,12]. Piperazine and its derivatives have also been investigated in broader pharmaceutical contexts [13]. These structural features provide a rationale for examining the DAI–PIP system. The molecular structures of daidzein and piperazine are shown in Figure 1.

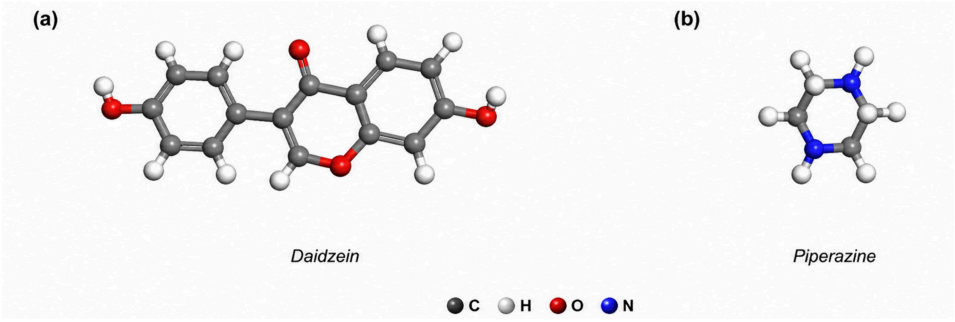


Figure 1. Molecular structures of (**a**) daidzein and (**b**) piperazine.

Several daidzein cocrystals have been investigated as a means of improving its physicochemical properties. Bhalla et al. prepared daidzein cocrystals with isoniazid, cytosine, and theobromine, which increased aqueous solubility by 2.1-, 1.9-, and 1.7-fold, respectively [8]. A DAI–PIP crystalline form was also reported to increase the equilibrium solubility of daidzein by up to 60.8-fold across four media [12]. These findings illustrate the potential of multicomponent crystallization in the solid-form development of poorly soluble compounds such as daidzein.

Despite growing interest in daidzein multicomponent solids, relatively few studies have examined systems formed with basic nitrogen-containing heterocycles such as piperazine. Their intermolecular interactions and associated low-frequency lattice dynamics also remain incompletely characterized. Terahertz time-domain spectroscopy (THz-TDS) is well suited to probing these phenomena [14] because terahertz photon energies (1 THz ≈ 4.1 meV) correspond to low-energy lattice vibrations and collective intermolecular modes. THz spectra can therefore provide distinctive signatures of molecular packing and the local lattice environment [15,16]. This sensitivity has supported applications of THz-TDS to pharmaceutical polymorphs, hydrates, and cocrystals [17,18].

Raman spectroscopy provides complementary information for cocrystal characterization. Conventional Raman measurements are particularly sensitive to intramolecular and functional-group vibrations, including shifts associated with API–coformer interactions, whereas THz spectroscopy preferentially probes low-frequency lattice vibrations

and collective intermolecular modes. Low-frequency Raman spectroscopy can also report lattice dynamics; accordingly, Raman and THz measurements offer complementary views of multicomponent crystal formation [15,19].

Temperature-dependent THz spectroscopy can provide additional insight into lattice dynamics through thermally induced peak sharpening, frequency shifts, peak splitting, and the emergence of spectral features. Wang et al., for example, investigated a naproxen–proline cocrystal over 2–17 THz and showed that temperature-dependent spectra, combined with quantum-chemical calculations, facilitated assignment of characteristic vibrational modes [20].

THz spectroscopy has been applied to both the identification and formation monitoring of pharmaceutical cocrystals. Ishihara et al. monitored the solid-state formation of an ibuprofen–nicotinamide cocrystal using THz and infrared spectroscopy with multivariate analysis [21]. Wang et al. combined THz spectroscopy with quantum-chemical calculations to examine supramolecular synthons in pyrazinamide–alkyl dicarboxylic acid cocrystals and identified stretching and twisting contributions to their collective vibrations [22]. Zhang et al. similarly used THz-TDS and density functional theory calculations to investigate composition-dependent spectral shifts and collective modes in methotrexate–histidine cocrystals [23]. Qin et al. demonstrated the complementary use of THz and Raman spectroscopy for structural investigation of a theophylline–nicotinamide cocrystal [19], while Yuan et al. monitored curcumin–pyrogallol cocrystal formation in real time and observed THz spectral changes consistent with PXRD results [24]. Collectively, these studies establish THz spectroscopy as a sensitive tool for distinguishing multicomponent crystalline forms, monitoring their formation, and probing their low-frequency lattice dynamics.

Previous studies have described a 1:1 DAI–PIP crystalline phase as a salt [6] and as a cocrystal [12]. Despite the different proton-transfer models, the reported structures have the same composition and space group and closely similar unit-cell parameters, PXRD patterns, and thermal behavior. Therefore, the prepared material is hereafter referred to as the DAI–PIP crystalline solid form. The reported system was reproduced by liquid-assisted grinding and examined primarily by THz-TDS, with complementary PXRD, DSC–TGA, and SEM characterization, to relate its low-frequency spectral response to changes in crystalline organization.

2. Materials and Methods

2.1. Materials

Daidzein (purity $\geq$ 97%) and anhydrous piperazine (purity $\geq$ 99%) were purchased from Shanghai Aladdin Biochemical Technology Co., Ltd. (Shanghai, China). methanol (purity 99.8%) was purchased from Shanghai Macklin Biochemical Technology Co., Ltd. (Shanghai, China). All materials were used as received.

2.2. Sample Preparation

The DAI–PIP crystalline solid form was prepared by liquid-assisted grinding, following the general approach used for mechanochemical preparation of pharmaceutical multicomponent solids [6,25,26]. The small amount of liquid added during grinding facilitates molecular diffusion and contact between the components and can promote solid-form conversion while limiting solvent consumption [25,26].

Daidzein and anhydrous piperazine were combined at a 1:1 molar ratio, consistent with the composition reported for the DAI–PIP crystalline phase [6,12]. Anhydrous piperazine (43.1 mg, 0.5 mmol) and daidzein (127.1 mg, 0.5 mmol) were accurately weighed using a precision electronic balance. Piperazine was stored and handled under conditions minimizing moisture exposure.

The weighed materials were transferred to a 50 mL zirconia grinding jar. Methanol (99.8%; 2–3 drops) and zirconia grinding balls (5 mm diameter) were added at a ball-to-material mass ratio of approximately 10:1. Preliminary handling showed pronounced agglomeration without methanol and formation of a wet slurry when excess methanol was used; accordingly, 2–3 drops were selected. The sample was processed in a planetary mill (JZDXQM-0.4L, JuZhongDa Intelligent Technology Co., Ltd., Changsha, China) at 400 rpm using three 10 min grinding periods separated by 5 min pauses, for a total grinding time of 30 min. The intermittent program limited local heating during milling.

After grinding, the sample was spread evenly in a glass Petri dish and vacuum-dried at 40 °C for 12 h to remove residual methanol. The dried material was gently dispersed, passed through a 50-mesh sieve, sealed, and stored in a desiccator until PXRD, thermal, THz-TDS, and SEM measurements.

2.3. PXRD

PXRD patterns of daidzein, anhydrous piperazine, and the DAI–PIP product were recorded using a D8 ADVANCE diffractometer (Bruker AXS GmbH, Karlsruhe, Germany) with Cu Kα radiation (λ = 1.5418 Å). The generator was operated at 40 kV and 30 mA. Data were collected over 5–50° 2θ at a scanning rate of 10°/min, with a step size of 0.02° and a dwell time of 0.12 s per step.

Each sample was spread evenly in a quartz sample holder and gently leveled with a glass slide. Measurements were performed at room temperature after instrument calibration.

The resulting patterns were compared to evaluate changes in crystalline organization after grinding.

2.4. DSC–TGA

The thermal behavior of daidzein, anhydrous piperazine, and the DAI–PIP product was measured using a simultaneous thermal analyzer (DZ-STA200, Nanjing Dazhan Instrument Co., Ltd., Nanjing, China).

Approximately 5–10 mg of each sample was placed in an open alumina crucible. Simultaneous DSC–TGA measurements were performed from 50 to 400 °C at a heating rate of 10 °C/min under flowing nitrogen (20 mL/min). For clarity, the DSC curves are presented over 50–350 °C, whereas the TGA curves are presented over the full measured range of 50–400 °C.

DSC curves were compared in terms of thermal events, and TGA curves were evaluated using the 5% mass-loss temperature (T5%), principal mass-loss regions, and residual mass at 400 °C. The thermal results were interpreted alongside the PXRD and THz-TDS data.

2.5. THz-TDS System

THz spectra were acquired using a laboratory-built THz-TDS system comprising a mechanical chopper, a Mai Tai femtosecond laser, and THz generation and detection modules. The laser operated at a center wavelength of 800 nm, a pulse width of 100 fs, and a repetition rate of 82 MHz. The laser output was divided into pump and probe beams. The pump beam illuminated an InAs crystal to generate THz pulses, which were collimated and focused through the sample using off-axis parabolic mirrors. The transmitted THz pulse and the probe beam were combined collinearly in a ZnTe electro-optic crystal, and the time-domain electric field was measured by electro-optic sampling of the probe-polarization change.

The effective instrumental range was 0.2–2.5 THz, with a spectral resolution of approximately 60 GHz (0.06 THz). A common displayed range of approximately 0.3–2.3 THz was used to compare the three samples; this range lies within the effective instrumental

bandwidth. The THz optical path was purged with nitrogen to suppress water-vapor absorption. The relative humidity in the chamber was maintained below 3%, and the measurement temperature was approximately 294 K.

For pellet preparation, each dry sample was mixed with high-density polyethylene (PE) powder at a 1:4 sample-to-PE mass ratio (30 mg sample and 120 mg PE) and homogenized by grinding. The mixture was pressed at 6.5 tons for 2 min. High-density PE was used as the dispersion matrix because of its negligible absorption in the measured THz range. Time-domain waveforms of the nitrogen-purged background and each sample were acquired sequentially. Fourier transformation yielded the corresponding amplitude and phase spectra, from which the optical parameters were calculated.

2.6. Scanning Electron Microscopy (SEM)

Powders of daidzein, anhydrous piperazine, and the DAI–PIP product were mounted on aluminum stubs using conductive double-sided carbon tape and sputter-coated with gold using an SD-900M ion sputter coater. Surface morphology was examined with a Hitachi S-4800 field-emission scanning electron microscope at an accelerating voltage of 10.0 kV and a working distance of 11.9 mm.

2.7. Data Processing Methods

Fabry–Pérot oscillations in the THz time-domain data were suppressed using an improved algorithm based on the Dorney–Fresnel formulation. A fast Fourier transform was then applied to obtain the amplitude and phase spectra. Using the measured sample thickness d, the refractive index n(ω) and absorption coefficient α(ω) were calculated using Equations (1) and (2), respectively.

$$n(\omega) = 1 + \phi(\omega)\frac{c}{\omega d} \tag{1}$$

$$\alpha(\omega) = -\frac{2}{d}\ln\left[\frac{\psi(\omega)[n(\omega)+1]^2}{4n(\omega)}\right] \tag{2}$$

In Equation (1), $\phi(\omega)$ denotes the phase difference between the sample and reference signals, d is the sample thickness, c is the speed of light, and ω is the angular frequency. In Equation (2), $\psi(\omega)$ is the ratio of the Fourier-transform amplitudes of the sample and reference signals; the remaining symbols are defined as above.

2.8. Theoretical Calculations

Density functional theory is an electronic-structure calculation method based on quantum mechanics. By solving the Schrödinger equation for a many-particle system, it enables atomic-level simulation of molecular geometries, lattice-vibrational modes, and spectral features. In THz spectroscopic studies, DFT can be used to simulate and assign the low-frequency collective vibrations of molecular crystals, thereby providing a physical interpretation of the experimental spectra [22,23].

In this study, periodic DFT lattice-dynamics calculations were performed using the CASTEP module of the Materials Studio 2020. The exchange–correlation energy was described using the Perdew–Burke–Ernzerhof (PBE) functional within the generalized gradient approximation (GGA). A plane-wave basis set with a kinetic-energy cutoff of 571.4 eV was employed, and the Brillouin zone was sampled using a 3 × 3 × 4 Monkhorst–Pack k-point grid. The geometry optimization and self-consistent-field calculations were performed using the Fine convergence criteria, and scalar-relativistic effects were treated using the Koelling–Harmon scheme. Frequency calculations were subsequently performed

based on the optimized periodic crystal structures to obtain the corresponding terahertz vibrational modes.

Based on the crystal-structure information obtained from the experimental PXRD patterns of DAI, anhydrous PIP, and DAI–PIP, initial periodic unit-cell models were constructed and fully geometrically optimized to obtain energetically stable structures. PXRD patterns were subsequently simulated from the optimized structures and compared with the corresponding experimental patterns. Their agreement supported the reasonableness of the optimized periodic crystal models and provided a structural basis for the subsequent THz spectral calculations. Phonon frequencies and infrared vibrational intensities were then calculated within the harmonic approximation to obtain the theoretical THz absorption spectra. The characteristic absorption features were assigned by comparing the experimental and calculated peak positions and analyzing the corresponding atomic-displacement vectors. This analysis revealed the contributions of functional-group vibrations, collective molecular motions, crystal packing, and intermolecular hydrogen-bond interactions to the low-frequency THz absorption features of DAI, PIP, and DAI–PIP.

3. Results and Discussion

3.1. PXRD Characterization

Powder X-ray diffraction was used to characterize the crystalline phases of DAI, anhydrous PIP, and the DAI–PIP product. PXRD reflects the long-range periodic arrangement of molecules in crystalline materials and can therefore be used to distinguish the DAI–PIP product from the two starting materials and to evaluate the reasonableness of the periodic crystal-structure models.

As shown in Figure 2, DAI exhibits characteristic reflections at 8.43°, 10.35°, 15.87°, 16.99°, 22.23°, and 24.51°, whereas anhydrous PIP exhibits reflections at 16.10°, 20.18°, 20.59°, 21.49°, and 27.56°. In the PXRD pattern of the DAI–PIP product, additional reflections appear at 18.62° and 23.19°, while the starting-material reflections at 10.35°, 16.99°, 21.49°, and 27.56° are no longer resolved. The appearance of additional reflections and the disappearance of several characteristic reflections of the starting materials indicate the formation of a DAI–PIP crystalline phase with a crystal-packing arrangement distinct from those of the starting materials after liquid-assisted grinding.

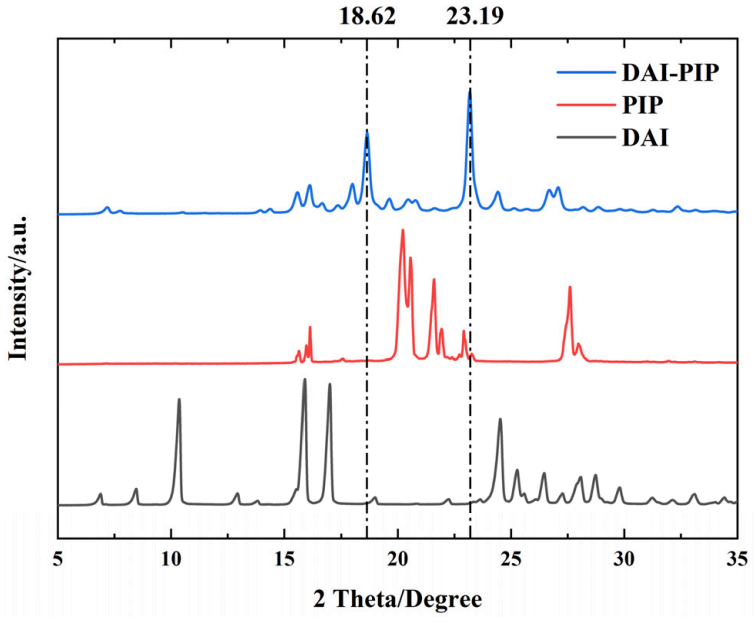


Figure 2. PXRD patterns of DAI, anhydrous PIP, and the DAI–PIP crystalline solid form. Patterns were acquired over 5–50° 2θ; the displayed range is 5–35° for clarity.

The experimental PXRD pattern of the DAI–PIP product is generally consistent with those previously reported for the 1:1 DAI–PIP crystalline phase [6,12]. In particular, the experimental reflection at 23.19° is close to the reflection at approximately 23.1° reported in both studies, while the reflection at 18.62° agrees with the reflection at 18.54° reported previously [12]. The good correspondence of these characteristic reflections further confirms that the DAI–PIP product prepared in this study exhibits crystallographic characteristics highly consistent with those of the previously reported 1:1 DAI–PIP crystalline phase.

To further assess the reasonableness of the periodic crystal-structure models used in the theoretical calculations, the PXRD patterns were simulated based on the DFT-optimized crystal structures. As shown in Figure 3, the experimental and simulated PXRD patterns of DAI, anhydrous PIP, and DAI–PIP are compared in panels (a), (b), and (c), respectively. The principal experimental reflections of each sample are reproduced in the corresponding simulated pattern, with good overall agreement in the characteristic peak positions.

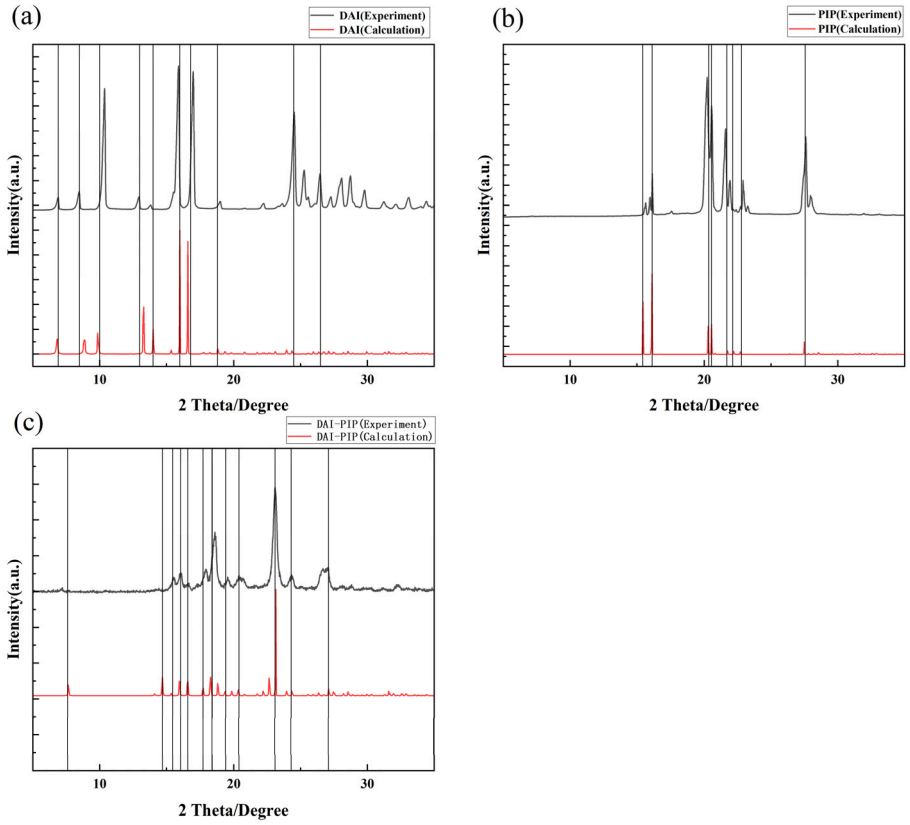


Figure 3. Comparison of the experimental and simulated PXRD patterns of (**a**) DAI, (**b**) anhydrous PIP, and (**c**) the DAI–PIP crystalline phase. The black and red curves represent the experimental and simulated patterns, respectively.

Some differences in relative peak intensities and peak positions are observed between the experimental and simulated PXRD patterns. The simulated patterns were calculated for ideal periodic crystal structures, whereas the experimental powder patterns may be influenced by preferred orientation, crystallite size, grinding-induced microstrain, and measurement temperature. These factors may cause changes in relative reflection intensities, slight peak shifts, and peak broadening without altering the correspondence between the principal characteristic reflections.

Overall, the good agreement between the experimental and simulated PXRD patterns validates the reasonableness of the DFT-optimized periodic crystal-structure models. Because the theoretical THz spectra and vibrational modes were calculated based on these

optimized structures, the PXRD comparison provides a structural basis for the reliability of the subsequent THz spectral simulations and vibrational-mode assignments.

3.2. DSC–TGA Characterization

Figure 4 compares the DSC curves of daidzein, anhydrous piperazine, and the DAI–PIP product. Daidzein exhibits a high-temperature endothermic event at approximately 322 °C. Because mass loss occurs over the corresponding temperature range in the TGA curve, this event is interpreted as a complex thermal event accompanied by mass loss. Anhydrous piperazine shows an endothermic melting peak at approximately 114 °C.

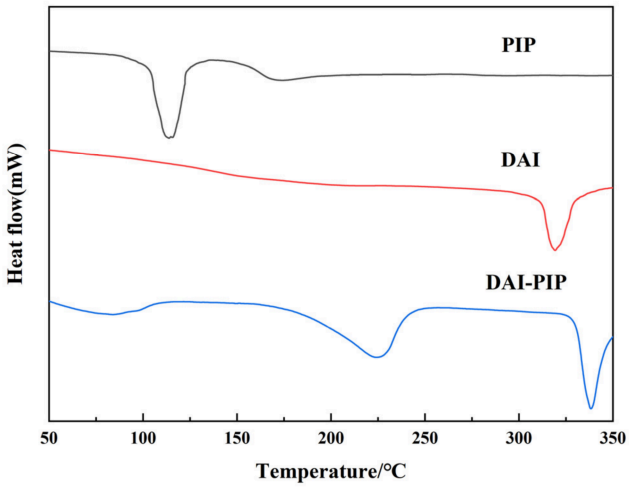


Figure 4. DSC curves of DAI, anhydrous PIP, and the DAI–PIP crystalline solid form, measured at 10 °C/min under nitrogen (20 mL/min). The displayed range is 50–350 °C.

The DAI–PIP product exhibits endothermic events at approximately 224 and 338 °C, indicating that its thermal behavior differs from that of the starting materials. The event near 224 °C occurs after the onset of mass loss at approximately 144 °C and may represent a composite process involving progressive volatilization of a piperazine-containing component and accompanying solid-state changes. The higher-temperature event is associated with the daidzein-containing residue, and the daidzein transition at approximately 322 °C is not resolved separately in the product curve. The piperazine melting peak at approximately 114 °C agrees with values of 115 and 112 °C reported previously [6] and [12], respectively. The product events at approximately 224 and 338 °C are also broadly consistent with those reported at 235 and 333 °C, respectively [12]; modest differences may reflect sample-preparation and measurement conditions.

Figure 5 compares the mass-loss profiles and residual masses of daidzein, anhydrous piperazine, and the DAI–PIP product. The temperature at which each sample had lost 5% of its initial mass is reported as T5%, providing a consistent measure for comparing the three profiles.

The T_5% values of daidzein, anhydrous piperazine, and the DAI–PIP product are approximately 281, 139, and 144 °C, respectively. Because anhydrous piperazine boils at approximately 145–146 °C, its mass loss under flowing nitrogen is attributed predominantly to volatilization. The comparable early mass loss of the DAI–PIP product is consistent with release of a volatile piperazine-containing component, potentially accompanied by minor contributions from residual methanol or absorbed moisture.

Daidzein undergoes its principal mass-loss stage above approximately 280 °C and retains approximately 55% of its initial mass at 400 °C. Anhydrous piperazine loses mass rapidly between approximately 130 and 230 °C and retains approximately 3%, consistent

with extensive volatilization under the measurement conditions. The DAI–PIP product exhibits two main mass-loss regions: the first begins at approximately 145 °C and is associated predominantly with loss of a piperazine-containing volatile component, whereas the second extends from approximately 280 to 380 °C and is associated with degradation of the daidzein-containing residue. The product retains approximately 30% of its initial mass at 400 °C.

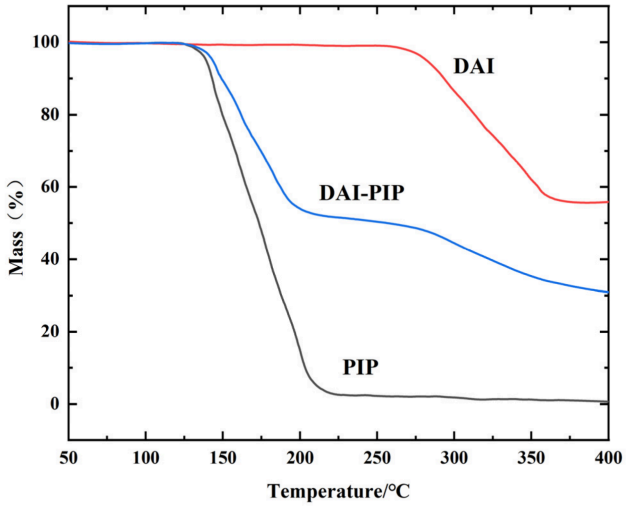


Figure 5. TGA curves of DAI, anhydrous PIP, and the DAI–PIP crystalline solid form, measured from 50 °C to 400 °C at 10 °C/min under nitrogen (20 mL/min).

The TGA profile therefore distinguishes the DAI–PIP product from either starting material and reveals sequential loss of a piperazine-containing component and degradation of the daidzein-containing residue.

3.3. THz Absorption Spectra and Simulation

Low-frequency THz absorption spectra of daidzein, anhydrous piperazine, and the DAI–PIP product were measured at room temperature and compared over a common displayed frequency range of approximately 0.3–2.3 THz. This range lies within the effective instrumental bandwidth of 0.2–2.5 THz and enables direct comparison of the low-frequency spectral characteristics among the three samples.

Figure 6 presents the THz absorption spectra of the three samples. The daidzein spectrum (Figure 6a) exhibits features at approximately 0.46, 1.02, 1.43, 1.69, and 2.28 THz. The anhydrous piperazine spectrum (Figure 6b) exhibits features at approximately 1.37, 1.87, and 2.22 THz.

The DAI–PIP product spectrum (Figure 6c) exhibits features at approximately 1.46, 1.84, and 2.28 THz. The 1.46 THz feature lies 0.03 THz above the DAI feature at 1.43 THz, while the 1.84 THz feature lies 0.03 THz below the PIP feature at 1.87 THz. Both differences are smaller than the instrumental resolution of approximately 0.06 THz and may therefore represent shifted, broadened, or overlapping contributions rather than separately resolved vibrational modes. The 2.28 THz feature coincides with the high-frequency feature observed for DAI.

Low-frequency THz spectra reflect collective vibrational behavior associated with molecular packing and intermolecular interactions. The THz-TDS spectra displayed in this study cover approximately 0.3–2.3 THz, which lies within the effective instrumental bandwidth of 0.2–2.5 THz and probes low-frequency lattice vibrations and collective molecular motions. The experimental absorption features are assigned below through

comparison with the periodic DFT-calculated spectra and atomic-displacement vectors presented in Figures 7–9 and Table 1.

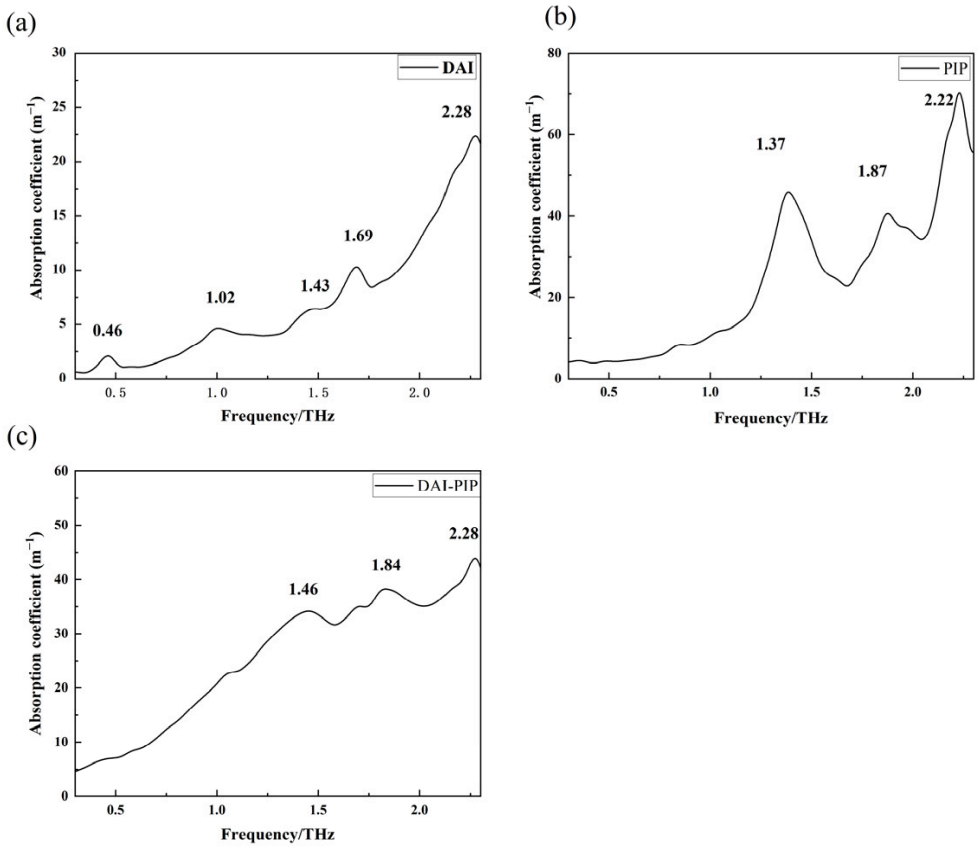


Figure 6. THz absorption spectra of (**a**) DAI, (**b**) anhydrous PIP, and (**c**) the DAI–PIP crystalline solid form in the range of approximately 0.3–2.3 THz.

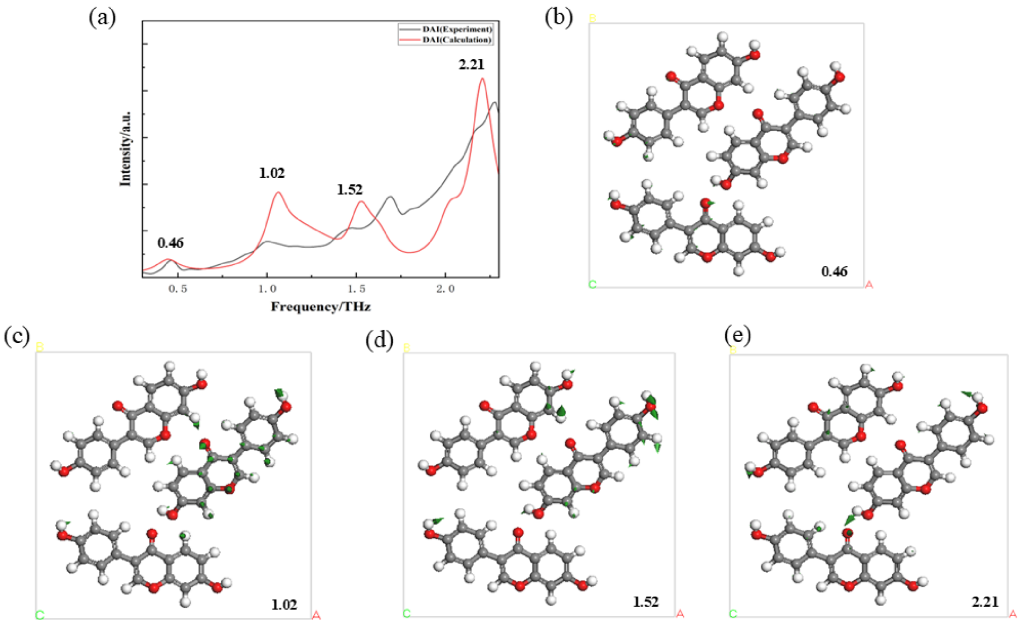


Figure 7. Comparison of THz spectroscopy and corresponding molecular vibration modes of DAI. (**a**) Experimental and simulated THz spectra of DAI; (**b**–**e**) vibration modes of DAI at 0.46, 1.02, 1.52, and 2.21 THz, respectively. The green arrows indicate the atomic displacement directions of the corresponding vibrational modes, and the uppercase letters A, B, and C denote the crystallographic axes.

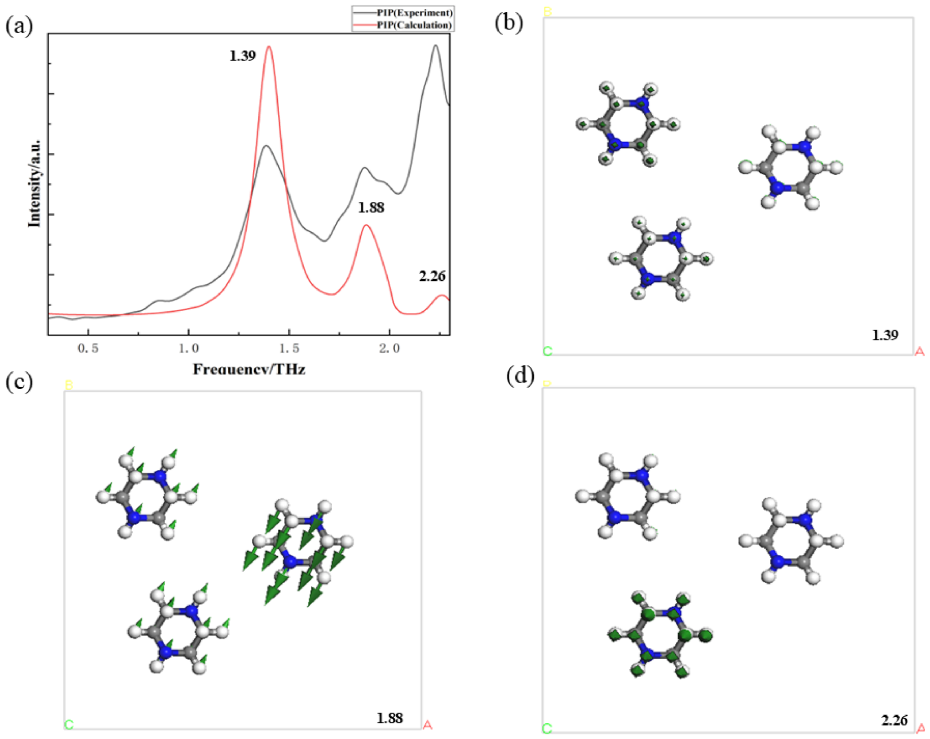


Figure 8. Comparison of THz spectroscopy and corresponding molecular vibration modes of PIP. (**a**) Experimental and simulated THz spectra of PIP; (**b**–**d**) vibration modes of PIP at 1.39, 1.88, and 2.26 THz, respectively. The green arrows indicate the atomic displacement directions of the corresponding vibrational modes, and the uppercase letters A, B, and C denote the crystallographic axes.

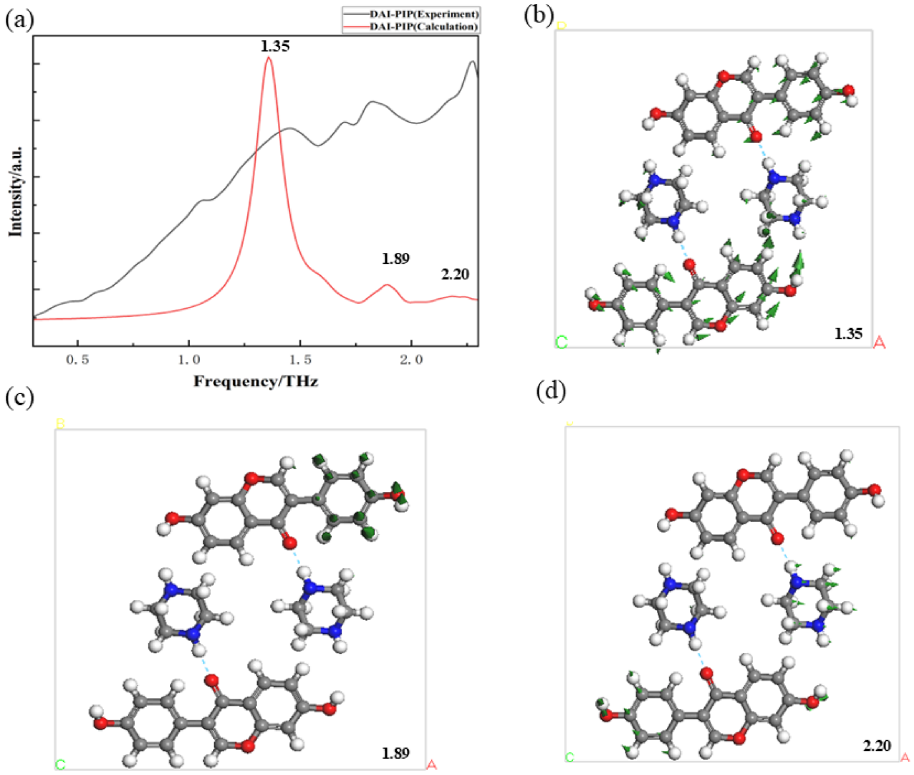


Figure 9. (**a**) Experimental and simulated THz spectra of DAI–PIP; (**b**–**d**) vibration modes of DAI–PIP at 1.35, 1.89, and 2.20 THz, respectively. The green arrows indicate the atomic displacement directions of the corresponding vibrational modes, the blue dashed lines represent hydrogen-bonding interactions, and the uppercase letters A, B, and C denote the crystallographic axes.

Table 1. Comparison of experimental and calculated THz peak positions and vibrational-mode assignments of DAI, PIP, and DAI-PIP.

Sample	Experimental Frequency (THz)	Calculated Frequency (THz)	|Δf| (THz)	Vibrational-Mode Assignment
DAI	0.46	0.46	0.00	Localized out-of-plane vibration of the –OH and C=O groups with participation of adjacent C–H groups
	1.02	1.02	0.00	Collective out-of-plane vibration of the entire DAI molecular group
	1.43	1.52	0.09	Localized coupled vibration dominated by the –OH groups, with contributions from the ring O atoms and adjacent molecular skeleton
	1.69	1.52	0.17	Possible splitting or overlapping contribution associated with the calculated mode at 1.52 THz
	2.28	2.21	0.07	Coupled vibration involving the –OH, C=O, and C–H groups and the aromatic skeleton of DAI
PIP	1.37	1.39	0.02	Collective out-of-plane vibration involving multiple PIP molecules
	1.87	1.88	0.01	Collective in-plane translational vibration of the PIP molecules
	2.22	2.26	0.04	Out-of-plane vibration dominated by one PIP molecule, involving the N–H and $–CH_2$ groups and the piperazine-ring skeleton
DAI-PIP	1.46	1.35	0.11	Relative in-plane vibration of the DAI and PIP molecular groups coupled with N–H···O hydrogen-bond deformation
	1.84	1.89	0.05	Localized in-plane vibration of the hydroxyl-substituted aromatic ring of one DAI molecule
	2.28	2.20	0.08	Coupled vibration of the PIP N–H and $–CH_2$ groups and piperazine-ring skeleton with the DAI –OH groups and aromatic skeleton, accompanied by N–H···O hydrogen-bond deformation.

To better understand the physical origins of the THz absorption features of DAI and their relationship with molecular vibrations, periodic DFT calculations were performed for the DAI crystal. Figure 7a compares the experimental and calculated THz spectra of DAI. The calculated absorption peaks are located at 0.46, 1.02, 1.52, and 2.21 THz, showing reasonable agreement with the principal features of the experimental spectrum. The corresponding vibrational modes are presented in Figure 7b–e. The absorption at 0.46 THz is mainly attributed to a localized coupled out-of-plane vibration of the oxygen-containing functional groups and adjacent C–H groups. The absorption at 1.02 THz primarily originates from a collective out-of-plane vibration of the entire DAI molecular group. The mode at 1.52 THz is dominated by the vibration of the –OH groups, with additional contributions from the ring O atoms and the adjacent molecular skeleton. The absorption at 2.21 THz is mainly assigned to a coupled vibration involving the –OH, C=O, and C–H groups and the aromatic skeleton of DAI. These assignments indicate that the THz absorption features of DAI involve both localized functional-group vibrations and collective motions of the molecular skeleton. In addition, intermolecular interactions and crystal packing may also influence the positions and profiles of these absorption features. It is noteworthy that the two experimental features at 1.43 and 1.69 THz correspond to a single calculated mode at 1.52 THz. This difference may arise because the DFT calculations were based on an ideal periodic crystal structure within the harmonic approximation, whereas the room-temperature experimental spectrum may additionally be affected by thermal motion, anharmonicity, crystal defects, and intermolecular interactions. Consequently, closely spaced vibrational contributions may appear as partially resolved features in the experimental spectrum but merge or overlap into a single absorption band in the calculated spectrum. Taken together, the calculated spectrum reasonably reproduces the principal features of the exper-

imental DAI spectrum and provides a theoretical basis for the corresponding vibrational-mode assignments.

Figure 8a compares the experimental and calculated THz spectra of PIP. The calculated absorption peaks are located at 1.39, 1.88, and 2.26 THz, corresponding well to the experimental peaks at 1.37, 1.87, and 2.22 THz, respectively. The corresponding frequency deviations are 0.02, 0.01, and 0.04 THz, all of which are smaller than the instrumental resolution of approximately 0.06 THz. The associated vibrational modes are shown in Figure 8b–d. The absorption at 1.39 THz is mainly attributed to a collective out-of-plane vibration involving multiple PIP molecules, in which the N–H and –CH_2 groups participate. The absorption at 1.88 THz primarily originates from a collective in-plane translational vibration of the PIP molecules, with the N–H and –CH_2 groups and the piperazine-ring skeleton moving approximately in the same direction. The absorption at 2.26 THz is mainly assigned to an out-of-plane vibration dominated by one PIP molecule, whereas the other PIP molecules exhibit substantially smaller displacement amplitudes. This mode involves the N–H and –CH_2 groups as well as the piperazine-ring skeleton. These assignments indicate that the characteristic THz absorption features of PIP arise from distinct collective motions of the PIP molecules. The close agreement between the experimental and calculated peak positions supports the proposed vibrational-mode assignments.

The simulated absorption spectrum shown in Figure 9a exhibits reasonable agreement with the experimental result. The calculated absorption peaks at 1.35, 1.89, and 2.20 THz correspond to the experimental features at 1.46, 1.84, and 2.28 THz, respectively. The optimized DAI–PIP structure contains intermolecular N–H···O hydrogen bonds between the N–H groups of PIP and the carbonyl O atoms of DAI, as indicated by the blue dashed lines in Figure 9b–d. The corresponding vibrational modes are presented in Figure 9b–d. For the 1.35 THz mode shown in Figure 9b, adjacent DAI molecular groups exhibit oppositely directed in-plane displacements, while the N–H and –CH_2 groups of PIP also participate in the motion. The relative motion of the DAI and PIP components is accompanied by deformation of the intermolecular N–H···O hydrogen-bond network. Therefore, this absorption peak is mainly attributed to a relative in-plane vibration of the DAI and PIP molecular groups coupled with hydrogen-bond deformation. In contrast, the atomic displacements of the 1.89 THz mode in Figure 9c are mainly localized on the hydroxyl-substituted aromatic ring of one DAI molecule, involving the –OH group, aromatic C–H groups, and the ring skeleton. This absorption peak is therefore assigned to a localized in-plane vibration of the hydroxyl-substituted aromatic ring of DAI. The 2.20 THz mode shown in Figure 9d involves the motion of the N–H and –CH_2 groups and the piperazine-ring skeleton of PIP, coupled with the vibration of the –OH groups and aromatic skeleton of DAI. The atoms associated with the intermolecular N–H···O hydrogen bonds also exhibit appreciable displacements, indicating that this mode is accompanied by hydrogen-bond deformation. These assignments indicate that the characteristic THz absorption features of DAI–PIP include both localized vibrations of the DAI component and coupled motions of DAI and PIP. In particular, deformation of the intermolecular N–H···O hydrogen bonds contributes to the calculated modes at 1.35 and 2.20 THz.

Overall, the periodic DFT-calculated spectra reasonably reproduce the principal experimental THz features of DAI, PIP, and DAI–PIP, as shown in Figures 7–9. The experimental and calculated peak positions, frequency deviations, and corresponding vibrational-mode assignments are summarized in Table 1. For DAI, the calculated peaks at 0.46 and 1.02 THz agree with the experimental peaks at the same frequencies, while the calculated peak at 2.21 THz corresponds to the experimental feature at 2.28 THz. The calculated mode at 1.52 THz is located between the experimental features at 1.43 and 1.69 THz, which may reflect mode splitting or the overlap of closely spaced vibrational contributions. For PIP, the

calculated peaks at 1.39, 1.88, and 2.26 THz correspond closely to the experimental peaks at 1.37, 1.87, and 2.22 THz, respectively. For DAI–PIP, the calculated peaks at 1.35, 1.89, and 2.20 THz correspond to the experimental features at 1.46, 1.84, and 2.28 THz, respectively. The vibrational-mode analysis indicates that the THz absorptions of DAI and PIP mainly originate from functional-group vibrations and collective molecular motions. For DAI–PIP, the calculated mode at 1.89 THz is mainly localized on the hydroxyl-substituted aromatic ring of DAI, while the modes at 1.35 and 2.20 THz involve coupled motions of DAI and PIP accompanied by intermolecular N–H···O hydrogen-bond deformation. The remaining differences between the experimental and calculated spectra may arise because the periodic DFT calculations describe ideal crystal structures within the harmonic approximation, whereas the experimental spectra are additionally affected by thermal motion, anharmonicity, crystal defects, and variations in crystal packing. Together with the good agreement between the experimental and simulated PXRD patterns, these results support the reasonableness of the periodic DAI–PIP crystal model and the interpretation of the product as a distinct hydrogen-bonded DAI–PIP crystalline phase rather than a simple physical mixture of DAI and PIP.

3.4. SEM

Figure 10 compares the particle morphologies of daidzein, anhydrous piperazine, and the DAI–PIP product. Daidzein consists mainly of rod- or plate-like particles with relatively smooth surfaces, whereas anhydrous piperazine forms irregular agglomerates. After liquid-assisted grinding, the DAI–PIP product appears as finer, relatively uniform particle aggregates, and the original rod-like morphology of daidzein is no longer readily distinguishable. These micrographs reveal particle-size reduction and changes in particle morphology and aggregation associated with the grinding process.

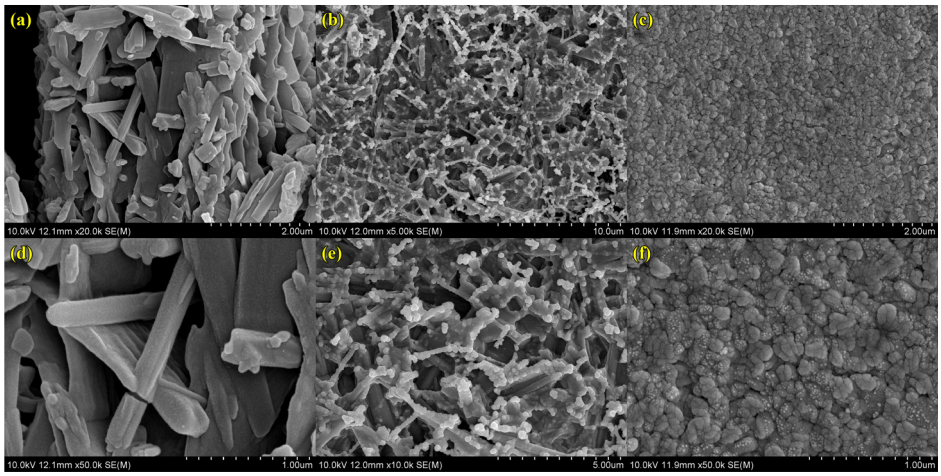


Figure 10. SEM images of the DAI–PIP crystalline solid form (**a**), anhydrous PIP (**b**), and DAI (**c**) at scales of 2 μm, 10 μm, and 2 μm, respectively, and of the DAI–PIP crystalline solid form (**d**), anhydrous PIP (**e**), and DAI (**f**) at scales of 1 μm, 5 μm, and 1 μm, respectively.

3.5. Integrated Solid-State Interpretation

The PXRD, thermal, THz-TDS, and SEM results consistently distinguish the ground DAI–PIP product from its starting materials. Its diffraction features agree with those reported for the 1:1 DAI–PIP crystalline phase, while its thermal profile and particle morphology reflect the reorganization and processing of the solid. Most notably, the THz spectrum adds low-frequency features to the existing characterization of this system. Taken together, the results support the presence of a DAI–PIP crystalline solid form closely related

to the previously reported phase and highlight THz-TDS as a complementary probe of its lattice-associated spectral response.

4. Conclusions

A DAI–PIP crystalline solid form was prepared by liquid-assisted grinding at a 1:1 starting-material molar ratio and characterized by PXRD, DSC–TGA, THz-TDS, and SEM. The PXRD pattern contained additional reflections at 18.62° and 23.19° and showed close correspondence with the previously reported DAI–PIP crystalline phase. DSC–TGA revealed distinct endothermic events and multistage mass-loss behavior, while SEM showed finer, relatively uniform particle aggregates after grinding.

THz-TDS revealed absorption features at approximately 1.46, 1.84, and 2.28 THz. Periodic DFT calculations reasonably reproduced these principal spectral features. Vibrational-mode analysis showed that the calculated mode at 1.89 THz is mainly associated with a localized vibration of the hydroxyl-substituted aromatic ring of DAI, whereas the modes at 1.35 and 2.20 THz involve coupled motions of DAI and PIP accompanied by intermolecular N–H···O hydrogen-bond deformation.

The combined diffraction, thermal, spectroscopic, and morphological results demonstrate consistent changes in solid-state behavior and provide a basis for further structural and lattice-dynamics studies of the DAI–PIP crystalline system.

Author Contributions: Conceptualization, Z.W.; methodology, H.S. and H.C.; validation, Z.W. and H.S.; formal analysis, H.S.; investigation, H.S.; resources, H.C., S.Z. and C.Z.; writing—original draft preparation, H.S.; writing—review and editing, H.C., Z.W. and H.S.; visualization, H.S. and H.C.; supervision, H.C., S.Z., B.S. and C.Z.; project administration, H.C.; funding acquisition, H.C. All authors have read and agreed to the published version of the manuscript.

Funding: This research was funded by the National Natural Science Foundation of China (NSFC), grant number 61575131, and the General Program of the Beijing Natural Science Foundation, grant number 4232066.

Institutional Review Board Statement: Not applicable.

Informed Consent Statement: Not applicable.

Data Availability Statement: The data used to support the findings of this study are available from the corresponding author upon request.

Acknowledgments: The authors thank Xinyi Bai for assistance with supplementary experiments and Kaidi Zhang for contributions during the early stage of this work.

Conflicts of Interest: The authors declare no conflicts of interest.

References

1. Guo, M.S.; Sun, X.J.; Chen, J.H.; Cai, T. Pharmaceutical cocrystals: A review of preparations, physicochemical properties and applications. *Acta Pharm. Sin. B* **2021**, *11*, 2537–2564. [CrossRef] [PubMed]
2. Qiao, N.; Li, M.Z.; Schlindwein, W.; Malek, N.; Davies, A.; Trappitt, G. Pharmaceutical cocrystals: An overview. *Int. J. Pharm.* **2011**, *419*, 1–11. [CrossRef] [PubMed]
3. Zhang, H.; Zeng, H.; Li, M.; Song, Y.; Tian, S.; Xiong, J.; He, L.; Liu, Y.; Wu, X. Novel Ascorbic Acid Co-Crystal Formulations for Improved Stability. *Molecules* **2022**, *27*, 7998. [CrossRef] [PubMed]
4. Duggirala, N.K.; Perry, M.L.; Almarsson, Ö.; Zaworotko, M.J. Pharmaceutical cocrystals: Along the path to improved medicines. *Chem. Commun.* **2016**, *52*, 640–655. [CrossRef] [PubMed]
5. Karimi-Jafari, M.; Padrela, L.; Walker, G.M.; Croker, D.M. Creating Cocrystals: A Review of Pharmaceutical Cocrystal Preparation Routes and Applications. *Cryst. Growth Des.* **2018**, *18*, 6370–6387. [CrossRef]
6. Meng, J.C.; Qiu, C.X.; Lu, C.Y.; He, X.; Zhao, X.H. A new crystalline daidzein-piperazine salt with enhanced solubility, permeability, and bioavailability. *Front. Pharmacol.* **2024**, *15*, 1385637. [CrossRef] [PubMed]

7. Singh, S.; Grewal, S.; Sharma, N.; Behl, T.; Gupta, S.; Anwer, M.K.; Vargas-De-La-Cruz, C.; Mohan, S.; Bungau, S.G.; Bumbu, A. Unveiling the Pharmacological and Nanotechnological Facets of Daidzein: Present State-of-the-Art and Future Perspectives. *Molecules* **2023**, *28*, 1765. [CrossRef] [PubMed]
8. Bhalla, Y.; Chadha, K.; Chadha, R.; Karan, M. Daidzein cocrystals: An opportunity to improve its biopharmaceutical parameters. *Heliyon* **2019**, *5*, e02669. [CrossRef] [PubMed]
9. Chinchu Praisthy, L.J.; Kushwah, R.; Dubey, S.; Kumar, V.; Jain, S. Pharmacotherapeutic potential of daidzein: Insights into mechanisms and clinical relevance. *Inflammopharmacology* **2025**, *33*, 5145–5171. [CrossRef] [PubMed]
10. Panizzon, G.P.; Bueno, F.G.; Ueda-Nakamura, T.; Nakamura, C.V.; Dias, B.P. Manufacturing Different Types of Solid Dispersions of BCS Class IV Polyphenol (Daidzein) by Spray Drying: Formulation and Bioavailability. *Pharmaceutics* **2019**, *11*, 492. [CrossRef] [PubMed]
11. Patel, R.V.; Park, S.W. An Evolving Role of Piperazine Moieties in Drug Design and Discovery. *Mini-Rev. Med. Chem.* **2013**, *13*, 1579–1601. [CrossRef] [PubMed]
12. Wang, Z.P.; Li, S.; Li, Q.; Wang, W.W.; Liu, M.R.; Yang, S.Y.; Zhang, L.; Yang, D.Z.; Du, G.H.; Lu, Y. A Novel Cocrystal of Daidzein with Piperazine to Optimize the Solubility, Permeability and Bioavailability of Daidzein. *Molecules* **2024**, *29*, 1710. [CrossRef] [PubMed]
13. Zheng, S.Y.; Lavrenyuk, K.; Lamson, N.G.; Fein, K.C.; Whitehead, K.A.; Dahl, K.N. Piperazine Derivatives Enhance Epithelial Cell Monolayer Permeability by Increased Cell Force Generation and Loss of Cadherin Structures. *Acs Biomater. Sci. Eng.* **2020**, *6*, 367–374. [CrossRef] [PubMed]
14. Pan, C. Multimodal characterization and density functional theory insights into the molecular structure and intermolecular interactions of the Aspirin–Ligustrazine cocrystal. *Int. J. Pharm.* **2025**, *683*, 126034. [CrossRef] [PubMed]
15. Wu, X.S.; Wang, Y.G.; Xue, J.D.; Liu, J.J.; Qin, J.Y.; Hong, Z.; Du, Y. Solid phase drug-drug pharmaceutical co-crystal formed between pyrazinamide and diflunisal: Structural characterization based on terahertz/Raman spectroscopy combining with DFT calculation. *Spectrochim. Acta A* **2020**, *234*, 118265. [CrossRef] [PubMed]
16. Zhang, X.; Zhu, Z.Q.; Bian, Y.J.; Zeng, R.N.; Zhou, W.L.; Yang, B. Combinatorial method to investigate cystine enantiomers using vibrational spectroscopies. *Infrared Phys. Techn* **2022**, *127*, 104406. [CrossRef]
17. Li, Q.; Bond, A.D.; Korter, T.M.; Zeitler, J.A. New Insights into the Crystallographic Disorder in the Polymorphic Forms of Aspirin from Low-Frequency Vibrational Analysis. *Mol. Pharm.* **2021**, *19*, 227–234. [CrossRef] [PubMed]
18. Yang, R.Z.; Chen, X.Q.; Wu, H.P.; Pang, W.T.; Zeng, X.L.; Huang, X.Y.; Li, Q.F.; Li, T.H.; Qin, B.Y. Vibrational spectroscopy investigation of ternary co-crystal formation of nitrofurantoin, nicotinamide and fumaric acid. *Spectrochim. Acta A* **2025**, *338*, 126215. [CrossRef] [PubMed]
19. Qin, B.Y.; Qiu, J.; Yang, R.Z.; Gan, Y.J.; Zhong, H.S.; Liao, Q.T.; Lu, S.L.; Li, Y. Structural Investigation of Cocrystal Formed Between Theophylline and Nicotinamide Based on Terahertz and Raman Spectroscopy. *IEEE Trans. Terahertz Sci. Technol.* **2024**, *14*, 476–483. [CrossRef]
20. Wang, P.F.; Han, W.F.; Wu, Y.; You, C.Q.; Zhang, C.Y.; Qu, Q.H.; Sun, X.H.; Yang, X.N.; He, M.X. Elucidating Molecular Vibrations within the Cocrystal of a Nonsteroidal Anti-Inflammatory Drug and Amino Acid by Temperature-Dependent Terahertz Spectroscopy at 2–17 THz: A Case Study. *Anal. Chem.* **2025**, *97*, 20743–20752. [CrossRef] [PubMed]
21. Ishihara, S.; Hattori, Y.; Otsuka, M.; Sasaki, T. Cocrystal Formation through Solid-State Reaction between Ibuprofen and Nicotinamide Revealed Using THz and IR Spectroscopy with Multivariate Analysis. *Crystals* **2020**, *10*, 760. [CrossRef]
22. Wang, P.F.; Li, Y.; Han, W.F.; Yan, Y.Y.; Zhang, C.Y.; Qu, Q.H.; Zhang, X.; Liu, L.Y.; Sun, X.H.; Yang, X.N.; et al. The supramolecular synthon behavior within cocrystals of pyrazinamide and alkyl dicarboxylic acids: A perspective from terahertz spectroscopy and quantum chemical calculation. *Talanta* **2024**, *278*, 126489. [CrossRef] [PubMed]
23. Zhang, Z.; Li, S.; An, H.; Tudi, R.; Song, X.; Zhou, M.; Zhang, F.; Shi, W.; Li, A.; Li, Z.; et al. Research on the cocrystal of methotrexate and histidine based on terahertz spectroscopy and DFT calculations. *Chem. Phys. Lett.* **2025**, *878*, 142334. [CrossRef]
24. Yuan, M.; You, C.; Zhang, C.; Zhao, S.; Yang, X.; Qu, Q.; Wang, P.; He, M. Tracking the cocrystal formation of curcumin and pyrogallol by terahertz spectroscopy. *CrystEngComm* **2025**, *27*, 5752–5760. [CrossRef]
25. Karki, S.; Friščić, T.; Jones, W.; Motherwell, W.D.S. Screening for Pharmaceutical Cocrystal Hydrates via Neat and Liquid-Assisted Grinding. *Mol. Pharm.* **2007**, *4*, 347–354. [CrossRef] [PubMed]
26. Solares-Briones, M.; Coyote-Dotor, G.; Páez-Franco, J.C.; Zermeño-Ortega, M.R.; de la O Contreras, C.M.; Canseco-González, D.; Avila-Sorrosa, A.; Morales-Morales, D.; Germán-Acacio, J.M. Mechanochemistry: A Green Approach in the Preparation of Pharmaceutical Cocrystals. *Pharmaceutics* **2021**, *13*, 790. [CrossRef] [PubMed]

Disclaimer/Publisher's Note: The statements, opinions and data contained in all publications are solely those of the individual author(s) and contributor(s) and not of MDPI and/or the editor(s). MDPI and/or the editor(s) disclaim responsibility for any injury to people or property resulting from any ideas, methods, instructions or products referred to in the content.